

This work was written as part of one of the author's official duties as an Employee of the United States Government and is therefore a work of the United States Government. In accordance with 17 U.S.C. 105, no copyright protection is available for such works under U.S. Law.

Public Domain Mark 1.0

<https://creativecommons.org/publicdomain/mark/1.0/>

Access to this work was provided by the University of Maryland, Baltimore County (UMBC) ScholarWorks@UMBC digital repository on the Maryland Shared Open Access (MD-SOAR) platform.

Please provide feedback

Please support the ScholarWorks@UMBC repository by emailing scholarworks-group@umbc.edu and telling us what having access to this work means to you and why it's important to you. Thank you.

RESEARCH ARTICLE

10.1002/2015JD023567

Key Points:

- Aerosol height is derived over wide areas from passive satellite sensors
- The present algorithm can be applied to both smoke and dust aerosols
- The retrieved height and SSA compare well with the CALIOP and AERONET data

Correspondence to:

J. Lee,
jaehwa.lee@nasa.gov

Citation:

Lee, J., N. C. Hsu, C. Bettenhausen, A. M. Sayer, C. J. Seftor, and M.-J. Jeong (2015), Retrieving the height of smoke and dust aerosols by synergistic use of VIIRS, OMPS, and CALIOP observations, *J. Geophys. Res. Atmos.*, 120, 8372–8388, doi:10.1002/2015JD023567.

Received 22 APR 2015

Accepted 22 JUL 2015

Accepted article online 25 JUL 2015

Published online 24 AUG 2015

Retrieving the height of smoke and dust aerosols by synergistic use of VIIRS, OMPS, and CALIOP observations

Jaehwa Lee^{1,2}, N. Christina Hsu¹, Corey Bettenhausen^{1,3}, Andrew M. Sayer^{1,4}, Colin J. Seftor^{1,3}, and Myeong-Jae Jeong⁵
¹NASA Goddard Space Flight Center, Greenbelt, Maryland, USA, ²Earth System Science Interdisciplinary Center, University of Maryland, College Park, Maryland, USA, ³Science Systems & Applications, Inc., Lanham, Maryland, USA, ⁴Goddard Earth Science Technology and Research, Universities Space Research Association, Columbia, Maryland, USA, ⁵Department of Atmospheric and Environmental Sciences, Gangneung-Wonju National University, Gangneung, Gangwon, South Korea

Abstract This study extends the application of the previously developed Aerosol Single-scattering albedo and layer Height Estimation (ASHE) algorithm, which was originally applied to smoke aerosols only, to both smoke and dust aerosols by including nonspherical dust properties in the retrieval process. The main purpose of the algorithm is to derive aerosol height information over wide areas using aerosol products from multiple satellite sensors simultaneously: aerosol optical depth (AOD) and Ångström exponent from the Visible Infrared Imaging Radiometer Suite (VIIRS), UV aerosol index from the Ozone Mapping and Profiler Suite (OMPS), and total backscatter coefficient profile from the Cloud-Aerosol Lidar with Orthogonal Polarization (CALIOP). The case studies suggest that the ASHE algorithm performs well for both smoke and dust aerosols, showing root-mean-square error of the retrieved aerosol height as compared to CALIOP observations from 0.58 to 1.31 km and mean bias from −0.70 to 1.13 km. In addition, the algorithm shows the ability to retrieve single-scattering albedo to within 0.03 of Aerosol Robotic Network inversion data for moderate to thick aerosol loadings (AOD of ~1.0). For typical single-layered aerosol cases, the estimated uncertainty in the retrieved height ranges from 1.20 to 1.80 km over land and from 1.15 to 1.58 km over ocean when favorable conditions are met. Larger errors are observed for multilayered aerosol events, due to the limited sensitivities of the passive sensors to such cases.

1. Introduction

Aerosol altitude is one of the key parameters required to better assess aerosol radiative effects, as it is critical for determining the vertical structure of the radiation field [Meloni *et al.*, 2005; Samset and Myhre, 2011; Zhang *et al.*, 2013; Choi and Chung, 2014]. Absorbing aerosols can significantly change the atmospheric heating rate, which in turn modulates the lifetime of adjacent clouds [Hansen *et al.*, 1997; Ackerman *et al.*, 2000; Koren *et al.*, 2008] and atmospheric stability [Penner *et al.*, 2003; Mishra *et al.*, 2014]. Height information can also be indicative of possible long-range transport of aerosols, due to the increased residence time and high wind speed in the free troposphere as compared to the planetary boundary layer [Williams *et al.*, 2002]. In addition, aerosol height information can improve air quality monitoring as aerosols at different altitudes can affect different targets, i.e., public health in the lower troposphere [van Donkelaar *et al.*, 2010] and air traffic in the upper troposphere [Song *et al.*, 2014].

Recent advances in satellite remote sensing (both in instrumentation and retrieval algorithms) have enabled the retrieval of aerosol height information from space; two major techniques are based on active lidar observations such as the Cloud-Aerosol Lidar with Orthogonal Polarization (CALIOP) [Winker *et al.*, 2007], and stereo imaging such as the Advanced Along-Track Scanning Radiometer (AATSR) [Fisher *et al.*, 2014] and Multi-angle Imaging Spectroradiometer (MISR) [Diner *et al.*, 1998]. The two remote sensing techniques are complementary in that CALIOP's active lidar can provide more complete vertical structure of aerosol layers but has a narrow footprint (~70 m), and thus, it has a limited detection rate of small-scale aerosol events near the source regions, while the (A)ATSR/MISR stereo imaging approach reports single representative heights in a wider swath width (several hundreds of kilometers) particularly near the source regions [Kahn *et al.*, 2008]. In addition, heavy aerosol loadings can cause saturation of the lidar signal, whereas the stereo imaging approach requires an aerosol plume that is optically dense enough to obscure the underlying terrain for better accuracy [Nelson *et al.*, 2013].

Table 1. Satellite Data Used for the ASHE Algorithm

Instrument	Data	Spatial Resolution (Nadir)	Swath Width
VIIRS	550 nm AOD, AE	6 km × 6 km	3040 km
OMPS	340–378 nm UVAI	50 km × 50 km	2800 km
CALIOP	Aerosol total backscatter coefficient, feature classification flag	70 m × 5 km	70 m

To further fill the gap between the two approaches, Jeong and Hsu [2008] developed the Aerosol Single-scattering albedo and layer Height Estimation (ASHE) algorithm which, as implied by its name, provides aerosol height information as well as single-scattering albedo (SSA) over wide areas using satellite measurements. The algorithm utilized aerosol products from multiple satellite sensors: aerosol optical depth (AOD) and Ångström exponent (AE) from the Moderate Resolution Imaging Spectroradiometer (MODIS), UV aerosol index (UVAI) from the Ozone Monitoring Instrument (OMI), and aerosol layer height from CALIOP. Briefly, the algorithm takes advantage of the sensitivity of UVAI to AOD, SSA, and aerosol layer height. It first retrieves SSA along the CALIOP swath by constraining the other two parameters using MODIS and CALIOP, and extends the height information outside of the CALIOP swath by assuming uniform SSA for the entire aerosol layer detected in a MODIS granule. If CALIOP observations are not available, the algorithm can still retrieve the height information with an assumed SSA, although in this case lower retrieval accuracy is expected.

One of the advantages of the algorithm is to retrieve aerosol height information for moderate to thick aerosol layers over broad areas, for which the CALIOP and (A)ATSR/MISR approaches have weaknesses. Therefore, it can help provide a more complete picture of global aerosol height, complementary to existing data sets. The original algorithm was only applied to smoke aerosols, since nonspherical dust resulted in a large uncertainty due to the spherical assumption in the forward models for AOD retrievals and UVAI calculations.

This study extends the application of the ASHE algorithm to both smoke and dust aerosols. The algorithm is applied to the aerosol products from Visible Infrared Imaging Radiometer Suite (VIIRS) and Ozone Mapping and Profiler Suite (OMPS) in place of MODIS and OMI, respectively. This will give us an opportunity to extend the data record beyond the Earth Observing System (EOS) era. Extensive updates have been made to the algorithm since its development, including but not limited to the incorporation of nonspherical dust properties in the forward model, use of the revised Collection 6 MODIS “Deep Blue” algorithm for VIIRS observations, an improved data collocation scheme, and the use of various aerosol profile shapes. This paper consists of the following sections: section 2 discusses the satellite data products used, section 3 describes methodology and updates made to the algorithm, section 4 provides several case studies for both smoke and dust events as well as uncertainty estimates, and section 5 provides a summary and discussions.

2. Data

As mentioned previously, the ASHE algorithm utilizes AOD, UVAI, and aerosol profile in its retrieval process. Table 1 summarizes the data sets used. The AOD/AE and UVAI data are from VIIRS and OMPS, respectively, which are both aboard Suomi National Polar-orbiting Partnership (S-NPP) satellite launched in October 2011. The aerosol profile is from CALIOP instrument aboard Cloud-Aerosol Lidar and Infrared Pathfinder Satellite Observatory (CALIPSO), available from June 2006 onward. Although on different platforms, collocations between the two satellites are not hard to achieve because of the similar equatorial crossing time (~13:30 local time for daytime orbital nodes) and wide swaths of VIIRS (3040 km) and OMPS (2800 km). In this study, data from July and August 2014 over North America are used for analysis of smoke events over land, and those from June to August 2013 over Atlantic Ocean are used for dust events over ocean.

2.1. VIIRS Deep Blue Aerosol Products

A revised version of the Collection 6 MODIS Deep Blue algorithm [Hsu *et al.*, 2013; Sayer *et al.*, 2013] is applied to measurements made by VIIRS to create the aerosol products (AOD and AE) over land surfaces. Over ocean we use an algorithm that has been used for various applications: retrieving aerosol properties from Geostationary Ocean Color Imager [Lee *et al.*, 2010b], testing effects of nonspherical dust models on AOD retrieval accuracy [Lee *et al.*, 2012], correcting for thin cirrus clouds in AOD retrievals [Lee *et al.*, 2013], and deriving aerosol direct radiative effects [Lee *et al.*, 2014]. This algorithm is expected to perform well particularly for dust cases as it includes nonspherical dust properties in the forward model; other aspects of the

algorithm are similar to other algorithms that have been applied to similar satellite sensors [e.g., Sayer *et al.*, 2012; Levy *et al.*, 2013]. Note that the same dust models will be included in an updated version of the SeaWiFS Ocean Aerosol Retrieval (SOAR) algorithm [Sayer *et al.*, 2012] for VIIRS, as preliminary investigations suggested that the dust models improved AOD retrieval accuracy for dust cases. The updated SOAR ocean data will be included alongside the Deep Blue land data in the operational NASA VIIRS Deep Blue data set, which is planned for public release in 2015.

One can find detailed descriptions for the land and ocean algorithms for MODIS in Hsu *et al.* [2013] and Lee *et al.* [2012], respectively. Brief summaries and updates made to the original algorithms are provided here. The algorithms presently take the NOAA format 86 s VIIRS sensor data records [Cao *et al.*, 2013] as input data and will be updated to take the NASA Level 1B data when they become available to use in the near future. The pixel size of the input VIIRS moderate resolution band (M-band) data is 750 m \times 750 m at nadir, and the aerosol products are provided at a nominal spatial resolution of 6 km \times 6 km (8 \times 8 pixels averaging). Aerosol properties are retrieved for cloud-free and snow-free pixels by finding the best match between observed and precalculated TOA reflectances stored as a function of solar/viewing geometries, AOD, aerosol optical models (SSA for land, and SSA and find-mode AOD fraction for ocean), and surface conditions (surface reflectance for land and wind speed for ocean). The lookup tables (LUTs) for land and ocean were calculated using the Dave radiative transfer code [Dave, 1972] and the VLIDORT code (linearized pseudo-spherical vector discrete ordinate radiative transfer model) [Spurr, 2006], respectively.

The Deep Blue land algorithm first retrieves spectral AOD at bands centered at 412, 488, and 672 nm, and derives AOD at 550 nm using the retrieved spectral AOD and AE calculated for a certain pair of wavelengths between the three. The selection of the wavelength pair depends on surface conditions, aerosol loading, and quality of the spectral AOD data.

The ocean algorithm determines AOD at 550 nm first together with aerosol models that best match the spectral reflectances at seven VIIRS bands centered at 488, 555, 672, 865, 1240, 1610, and 2250 nm. The LUT is created for AOD referenced to 550 nm, with varying spectral shapes according to the aerosol model assumed. The spectral AOD can then be recalculated based on the retrieved AOD at 550 nm, aerosol model, and the residues of the spectral fitting. In contrast to the land algorithm, AE over ocean is defined over a fixed wavelength pair 488–865 nm. Since the ASHE algorithm utilizes AOD at 550 nm, AOD hereafter indicates the value at 550 nm unless otherwise stated. It should be noted that four consecutive (86 s) VIIRS granules are stitched together before applying the ASHE algorithm to better capture large-scale aerosol events.

The quality of the AOD products is evaluated as compared to the Aerosol Robotic Network (AERONET) [Holben *et al.*, 1998] direct-sun measurements for a period from March 2012 to November 2013. The cloud-screened and quality-assured Level 2.0 data [Smirnov *et al.*, 2000] from all of the AERONET sites over North America (24°N \sim 56°N, -130° E \sim -60° E) and Capo Verde are used for the land and ocean algorithms, respectively. For the land algorithm, only data passing recommended quality flag checks for the “vegetated” retrieval path [Hsu *et al.*, 2013] are used, as the algorithm is applied to the summer season over North America where vegetated retrievals are dominant. No additional quality control is applied to the ocean data. The AERONET and VIIRS data are collocated and averaged within a temporal window of ± 30 min of the VIIRS overpass time and a spatial window of 25 km from the AERONET locations, respectively. Only data points with the number of collocations larger than 1 for AERONET and 10% of all of the possible pixels for VIIRS are compared. Figure 1 reveals that the Deep Blue algorithm performs well for the VIIRS sensor, showing 78% of the points falling within the expected error [$\pm(0.03 + 0.2\tau)$], with a small mean bias (MB; -0.01) and root-mean-square error (RMSE; 0.05). The ocean algorithm also shows promising performance for dust cases due to its improved handling of nonspherical dust particles, resulting in 80% of the data points falling within the expected error [$\pm(0.03 + 0.05\tau)$], with a negligible MB and small RMSE (0.04).

2.2. OMPS UVAI

UVAI has widely been used in detecting UV-absorbing aerosols in the atmosphere, such as smoke and dust [Hsu *et al.*, 1996; Herman *et al.*, 1997; Torres *et al.*, 1998; Jeong and Li, 2005; Kim *et al.*, 2007; Torres *et al.*, 2013]. The UVAI is known to be sensitive to aerosol layer height as well as AOD and SSA [Hsu *et al.*, 1999]. Therefore, it can be used to provide aerosol height information when the other parameters are constrained using other

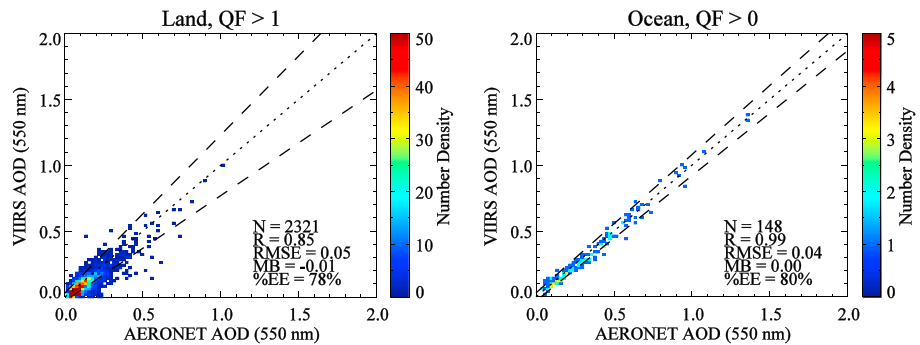


Figure 1. Scatterplots of AOD between AERONET observations and VIIRS retrievals (left) over North America for the land algorithm and (right) at Capo Verde for the ocean algorithm for a period from March 2012 to November 2013. The dashed lines are expected error confidence interval of $\pm(0.03 + 0.20\tau)$ for land and $\pm(0.03 + 0.05\tau)$ for ocean, where τ is AOD. The statistics shown are the number of data points (N), Pearson coefficient (R), mean bias (MB), root-mean-square error ($RMSE$), and fraction of data points falling within the expected error ($\%EE$).

data sources. This study utilizes the ozone nonabsorbing 340–378 nm wavelength pair to calculate UVAI from the OMPS measurements [Seftor *et al.*, 2014]:

$$UVAI(\tau_a, \omega_0, z_a) = -100 \times \left\{ \log_{10} \left[\left(\frac{I_{340}}{I_{378}} \right)_{\text{meas}} \right] - \log_{10} \left[\left(\frac{I_{340}}{I_{378}} \right)_{\text{calc}} \right] \right\},$$

where τ_a , ω_0 , and z_a represent AOD, SSA, and aerosol layer height, respectively, and I_{meas} and I_{calc} are measured and calculated TOA radiances at wavelengths represented by the subscripts. The calculated radiance at the shorter wavelength represents a Rayleigh atmosphere with the Lambertian-equivalent reflectivity (LER) derived at the longer wavelength. Since the LER is derived by matching TOA radiances between observed and calculated values as a function of LER for cloud-free, Rayleigh atmosphere, the measured and calculated TOA radiances at the longer wavelength are the same.

OMPS provides measurements at a nominal spatial resolution of about $50 \text{ km} \times 50 \text{ km}$ at nadir in normal operations; once a week measurements are taken at a higher resolution of $12 \text{ km} \times 12 \text{ km}$ at nadir. Although the same approach can be applied to the high-resolution data as well, this study only considers data from the normal operational mode.

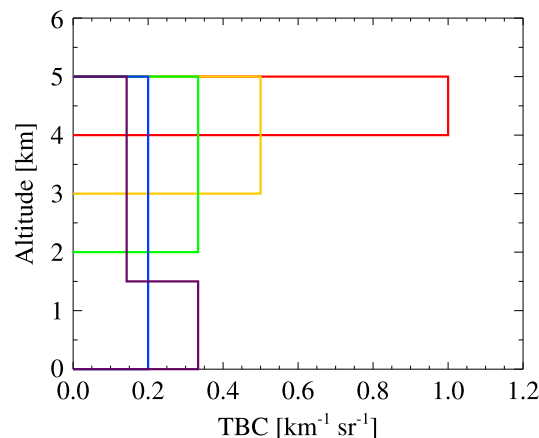


Figure 2. Five different aerosol profile shapes assumed in the retrieval process. A column-integrated TBC of 1.0 sr^{-1} and ATH of 5 km are assumed. Colors are for uniform aerosol layers with geometric thickness of 1 km (red), 2 km (yellow), 3 km (green), and reaching surface (blue) and aerosol layer with half of the AOD in the free troposphere and the other half in the boundary layer (purple).

2.3. CALIOP Aerosol Profile

It is important to handle the aerosol vertical profile (both altitude and shape) correctly in the ASHE algorithm because UVAI has sensitivity to both of these properties. The original algorithm assumed a single Gaussian shape for elevated smoke layers, which was appropriate for typical smoke cases. However, to extend the application to dust layers, which can occur in more variable profile shapes, we include five different profile shapes in the forward model as a function of aerosol top height (hereafter ATH), i.e., four kinds of uniform aerosol layers (with geometric thickness of 1, 2, and 3 km, and reaching surface) and an additional profile with half of the AOD in the free troposphere (above 1.5 km) and the other half in the boundary layer (below 1.5 km). Figure 2 illustrates the five different profile shapes for an assumed aerosol layer with a column-integrated aerosol total backscatter coefficient (TBC) of 1.0 sr^{-1} and ATH of 5 km.

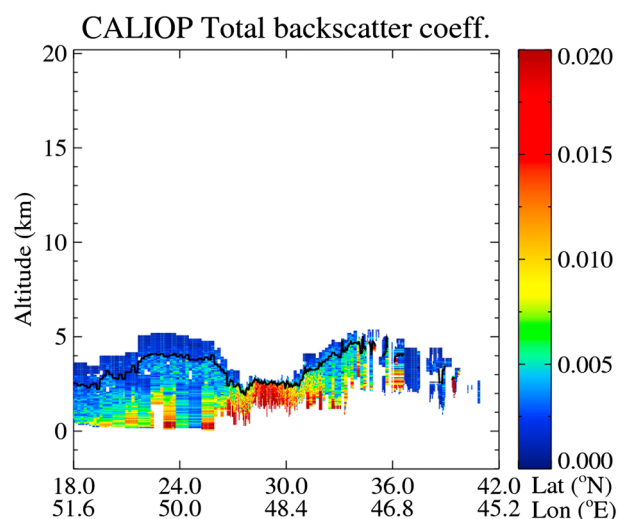


Figure 3. An example of the CALIOP TBC profile and ATH (solid line) determined by the procedure described. Data are for a dust event observed over the Arabian Peninsula on 1 June 2013.

We examined the sensitivity of UV radiances to profile shapes (i.e., uniform vs. Gaussian shape) to investigate potential errors from using a uniform profile instead of a Gaussian, which is known to be suitable for smoke layers. The result showed that the sensitivity to geometric thickness (1 km vs. 2 km) is ~ 1000 times larger than sensitivity to the profile shape for a typical smoke case with AOD of 1.0, SSA of 0.9, ATH of 5.0 km, and geometric thickness of 1 km. The sensitivity to profile shape increases with geometric thickness but remains an order of magnitude or more smaller than the sensitivity to the geometric thickness. Visual inspection of TBC profiles for smoke cases suggests that the Gaussian approximation does not hold well for geometrically thick smoke layers. Thus, it can be inferred that the uniform assumption would not result in significant error.

With the inclusion of different aerosol input profiles in the LUTs, it now becomes necessary to determine ATH and aerosol profile shape from the CALIOP observations. To minimize the effects of the assumed lidar ratio for different aerosol types on the profile shape, we use the TBC profile in the “CAL_LID_L2_05kmApro” product, which does not include aerosol type-specific lidar ratio information, as compared to the extinction coefficient profile, which does require a lidar ratio assumption. The ATH is taken as the altitude reached after descending a TBC of $0.03 \text{ km}^{-1} \text{ sr}^{-1}$ from the top of the TBC profile, to minimize potential errors caused by optically thin elevated layers above the layer of interest. The TBC of $0.03 \text{ km}^{-1} \text{ sr}^{-1}$ corresponds to AOD of about 0.10 given CALIOP’s vertical resolution of 60 m and an assumed lidar ratio of 55 (which is intermediate between those for dust and smoke defined in the CALIOP operational data processing) [Omar *et al.*, 2009]. Then, a least squares method matching observed and assumed aerosol profiles is used to select the most appropriate profile shape from the five options listed above.

Figure 3 shows an example of the CALIOP TBC profile with the ATH determined by the procedure described above. The top height is not defined if the column-integrated TBC value is less than $0.1 \text{ km}^{-1} \text{ sr}^{-1}$ (AOD of ~ 0.3), cloud pixels determined by the “feature classification flag” product are present close to the determined ATH ($< 200 \text{ m}$), or there are obvious distinct multiple aerosol layers (distance between any two consecutive TBC pixels $> 1 \text{ km}$).

3. Method

The ASHE algorithm basically utilizes the sensitivity of UVAI to AOD, SSA, aerosol type (size distribution and wavelength dependence of SSA), and aerosol profile. Therefore, any one of the parameters can be retrieved using UVAI when the others are properly constrained. In this study, since the target parameter is the height information, AOD, SSA, and aerosol type need to be constrained from other data sources.

Figure 4 shows the flowchart of the ASHE algorithm. In order to merge the data from different sensors, we first start with collocations of the various data sets. Since VIIRS and OMPS are on the same platform, temporal matching between the two sensors is not necessary. However, due to the difference in orbits between S-NPP and CALIPSO, a temporal window of 1 h is used to matchup S-NPP and CALIOP data. When there are multiple CALIOP swaths within a VIIRS/OMPS granule, all of the collocated data are used in the retrieval process.

Spatial matching is more difficult to achieve because of the large difference in pixel size between VIIRS ($6 \text{ km} \times 6 \text{ km}$) and OMPS ($50 \text{ km} \times 50 \text{ km}$). Furthermore, the difference increases with the scan angle. The original algorithm aggregated OMI pixels ($13 \text{ km} \times 24 \text{ km}$) into MODIS pixels ($10 \text{ km} \times 10 \text{ km}$) with a spatial window of 0.2° , but the same procedure is found to result in large errors for VIIRS and OMPS data because

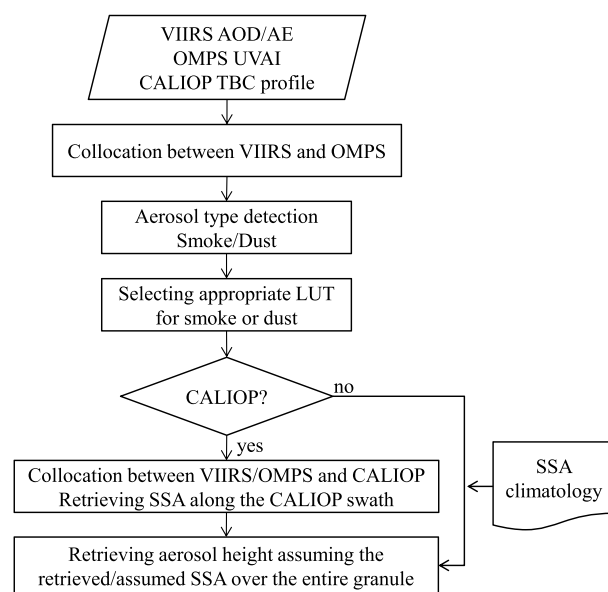


Figure 4. Flowchart of the ASHE algorithm.

Using 30×30 subpixels provides a relaxed criterion, yielding the most accurate collocation that can be achieved from the suggested method over the entire VIIRS/OMPS granule. Our investigation suggests that the new method results in better performance with a significantly reduced “checkerboard effect” as compared to the original method.

For CALIOP, the data within 100 km of OMPS pixels are aggregated, but not averaged, for each CALIOP pixel to be used in the retrieval process. This is to reduce errors that can possibly be caused by sharp boundaries of aerosol layers. The 100 km distance was chosen to account for the increased pixel size of OMPS UVAI data at extreme scan angles ($\sim 200 \text{ km} \times \sim 100 \text{ km}$).

The next step is to constrain the aerosol type using the collocated VIIRS and OMPS data sets. For pixels with $\text{AOD} > 0.3$, UV-absorbing aerosols, such as smoke and dust, are determined by requiring a $\text{UVAI} > 0.7$, and the smoke and dust aerosols are separated from each other by AE values based on their general size distribution (smoke: $\text{AE} > 1.2$; dust: $\text{AE} < 0.8$) [Jeong and Li, 2005; Kim et al., 2007]. The ASHE algorithm is only applied to pixels determined as smoke or dust, and the aerosol type information is used to select the proper LUTs for the respective cases.

When a complete set of VIIRS (AOD and AE), OMPS (UVAI), and CALIOP (aerosol profile) aerosol products are available, together with the aerosol type information determined in the previous step, the ASHE algorithm first retrieves 340 nm SSA along the CALIOP swath by comparing the observed and precalculated UVAIs. Since the LUTs were created as a function of solar/viewing geometry, AOD, SSA, ATH, profile shape, and surface elevation for respective smoke or dust aerosol models (Table 2), and all of the other parameters except SSA can be constrained by the VIIRS and CALIOP aerosol products, the UVAI can now be expressed as a function of SSA only, and thus, the SSA can be retrieved. A linear interpolation is used for the LUT to match the observed UVAI for all of the parameters except profile shape, for which the five discrete values are used.

In this application, one smoke and one dust model as a function of SSA are assumed in the forward model to calculate UVAI, i.e., no change in size distribution for each model in contrast to the original algorithm. In the original algorithm, the LUT was calculated as a function of SSA and AE to be used according to the retrieved AE from MODIS. However, large uncertainty in the retrieved AE, particularly over land surfaces, limited its usefulness in the retrieval process as compared to using a representative size distribution. As a result, it was omitted in this application. However, this can readily be updated when a more accurate AE product becomes available. The aerosol properties used in the forward model are summarized in Table 3.

When SSA is retrieved along the CALIOP swath, using the approach above, ATH can be retrieved outside of the CALIOP swath by assuming a uniform SSA for the entire smoke or dust layers detected in a VIIRS granule.

OMPS pixels are much larger than those of VIIRS. To overcome this issue, the collocation is performed based on a pixel dimension rather than the center points of the pixels, and VIIRS pixels are aggregated into OMPS pixels rather than the other way around. Specifically, we divide each OMPS pixel into 30×30 subpixels and aggregate the VIIRS pixels into each subpixel that minimizes the distance between the VIIRS pixels and the subpixel. The distance is calculated based on the center points of the VIIRS pixels and the OMPS subpixels. After performing the collocation for all of the OMPS subpixels, any overlapped VIIRS pixels are discarded to avoid redundancy, and the remaining data are averaged. The number of OMPS subpixels is adjustable according to desired calculation time vs. accuracy; i.e., the larger the number of subpixels, the better the collocation accuracy.

Table 2. LUT Node Points for the Forward Model^{a,b}

Variables	# of Nodes	Nodes
SZA	9	0°, 10°, ..., 80°
VZA	9	0°, 10°, ..., 80°
RAA	19	0°, 10°, ..., 180°
AOD (550 nm)	9	0.0, 0.1, 0.3, 0.5, 1.0, 2.0, 3.0, 4.0, 5.0
SSA (340 nm)	7	0.7, 0.75, ..., 1.0
ATH	7	1, 2, 3, 5, 7, 10, 15 km
Profile shape	5	4 uniform shapes with varying geometric thickness and half in the free troposphere + half in the boundary layer
Surface elevation	2	0, 3 km

^aThe same node points are used for smoke and dust aerosol models.

^bSZA: solar zenith angle, VZA: viewing zenith angle, RAA: relative azimuth angle.

In this application, a median SSA and the most frequently detected profile shape are taken to represent the entire aerosol layers. If the CALIOP data are not available for a certain aerosol event, the ATH can still be retrieved using an assumed SSA (e.g., a SSA climatology from ASHE and/or AERONET retrievals) at a cost of increased error. However, we only focus on aerosol events for which the CALIOP data are available, as creating the climatology requires long-term global data processing, which is beyond the scope of this study.

Although the retrieved SSA is at 340 nm, it can be converted to other wavelengths (378, 412, 445, 555, and 672 nm in this application) based on the aerosol models used for comparison purposes with available data sets (e.g., AERONET). We take the Level 2.0 (for dust cases) or 1.5 (for smoke cases as Level 2.0 data are not available at the present time) Version 2 AERONET inversion data [Dubovik and King, 2000; Dubovik et al., 2006] to compare the retrieved SSA. The AERONET data are averaged within 2 h temporal window of the VIIRS overpass time to be compared. Although they are retrieved products rather than measurements, so should not be considered as validation target, the inversion product provides SSA at 440, 675, 870, and 1020 nm with an uncertainty of 0.03 for 440 nm AOD > 0.5 and solar zenith angle > 50° [Dubovik et al., 2000]. Lower uncertainties are expected for higher AOD conditions, on which the present application mostly focuses.

4. Results

4.1. Application to Wildfire Smoke Aerosols Over North America

Significant wildfire activity was observed in the western part of North America, extending from Oregon in the United States up to the Northwest Territories in Canada, from July to August 2014. The ASHE algorithm was applied to these wildfire cases during the whole 2 month period; the results shown here highlight the strengths and weaknesses of the algorithm.

Figure 5 shows a smoke event observed on 16 July 2014. In this case, thick smoke layers are clearly seen in the RGB image, with AOD ranging from about 0.5 to higher than 1.5. The corresponding high UVAI values also indicate the presence of UV-absorbing aerosols in the region. The MODIS fire mask [Giglio et al., 2003] suggests that there are quite a few source locations scattered over the region while showing major sources at latitudes and longitudes of around 52°N to 56°N and −120°E to −125°E, respectively. The different

Table 3. Microphysical Properties for the Smoke and Dust Aerosols Used in the Forward Model, Where n Is the Real Part of Refractive Index, r and σ Are Mode Radius and Geometric Standard Deviation, Respectively, for Bimodal Lognormal

Volume Size Distributions, $\frac{dV(r)}{d \ln r} = \sum_{i=1}^2 \frac{C_{v,i}}{\sqrt{2\pi}\sigma_i} e^{-\frac{1}{2} \left(\frac{\ln r - \ln r_{vi}}{\sigma_i} \right)^2}$, FMF Is Fine-Mode AOD Fraction at 550 nm, and AAE Is Absorption AE ^a							
Aerosol Type	n	$r_{v1}; r_{v2}$ (μm)	$\sigma_1; \sigma_2$ (μm)	FMF	AE (340–550 nm)	AAE (340–378 nm)	Particle Shape
Smoke	1.47	0.15; 3.25	0.40; 0.75	0.85	1.33–1.56	1.6	Sphere
Dust	1.48	0.15; 1.90	0.40; 0.63	0.15	0.27–0.28	2.0	Spheroid mixture ^b

^aThe volume concentrations (C_v) of the fine- and coarse-mode are scaled with respect to AOD and FMF in the radiative transfer model. The spectral imaginary refractive index varies according to the SSA node points and AAE.

^bCf. Dubovik et al. [2006]; Meng et al. [2010]; Lee et al. [2012].

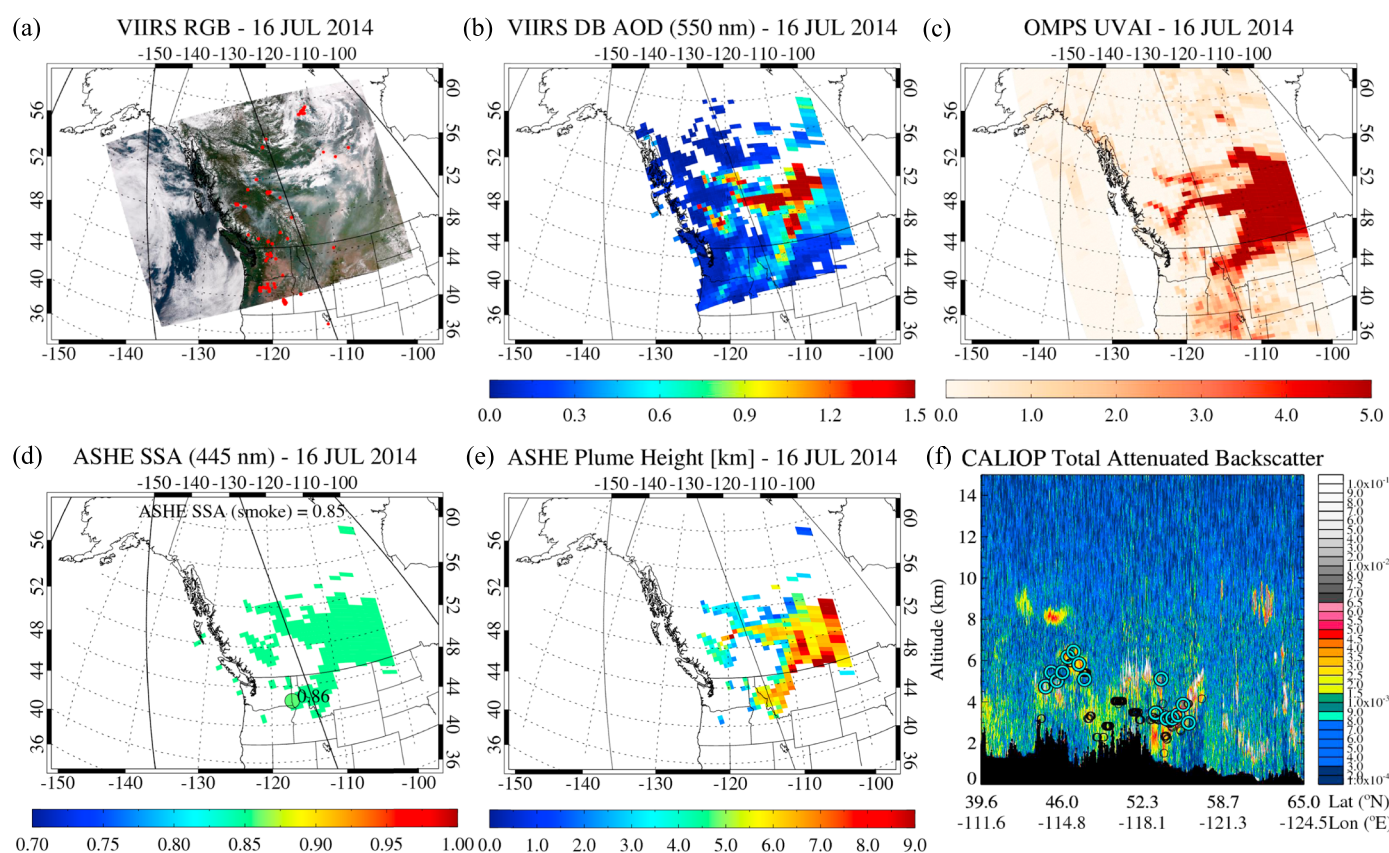


Figure 5. Application of ASHE to a smoke event observed over North America on 16 July 2014. Plots shown are (a) VIIRS RGB image with MODIS/Aqua fire mask (MYD14) in red dots, (b) VIIRS Deep Blue AOD, (c) OMPS UVAI, (d) retrieved SSA and (e) ATH from ASHE, and (f) CALIOP total attenuated backscatter (TAB) profile with CALIOP-derived (black circle) and ASHE-retrieved ATHs (cyan circle).

geometric shapes of the plumes (one stretching from east to west and another from north to south) suggest that these plumes are likely from different sources and/or different transport paths.

For the smoke plumes originating from different sources, ASHE retrieves a single 445 nm SSA of 0.85, which is comparable to the 440 nm SSA at the nearby AERONET site (0.86). The retrieved ATH suggests that the smoke plumes generally reside at lower altitudes (2 to 4 km) near the source region and increase during transport to the east (up to 6 to 9 km). This horizontal variability cannot be detected by CALIOP due to its narrow swath. The retrieved ATH shows high agreement with that from the CALIOP TBC profile, showing RMSE of 0.79 km and MB of 0.25 km (Table 4). This suggests that the uniform SSA assumption works well for this complicated smoke event (i.e., multiple sources). It is worthwhile to note that the retrieved ATH does not show strong biases over mountainous areas, as the algorithm accounts for the surface elevation in its retrieval process. The large bias observed at latitudes of around 45°N is partly due to the multiple aerosol layers (one at 5 km and another at 8 km) and also due to a potential high bias in AOD over the snow-covered areas.

Table 4. Comparison Statistics Between ASHE-Retrieved and CALIOP-Derived ATHs for Smoke Cases

Aerosol Type	Date	Mean ATH (km)		RMSE (km)	MB (km)
		CALIOP	ASHE		
Smoke	16 July 2014	3.83	4.12	0.79	0.25
	30 July 2014	3.55	3.79	0.69	0.37
	06 August 2014	2.78	3.17	0.69	0.36
	07 August 2014	2.54	4.72	1.31	1.13

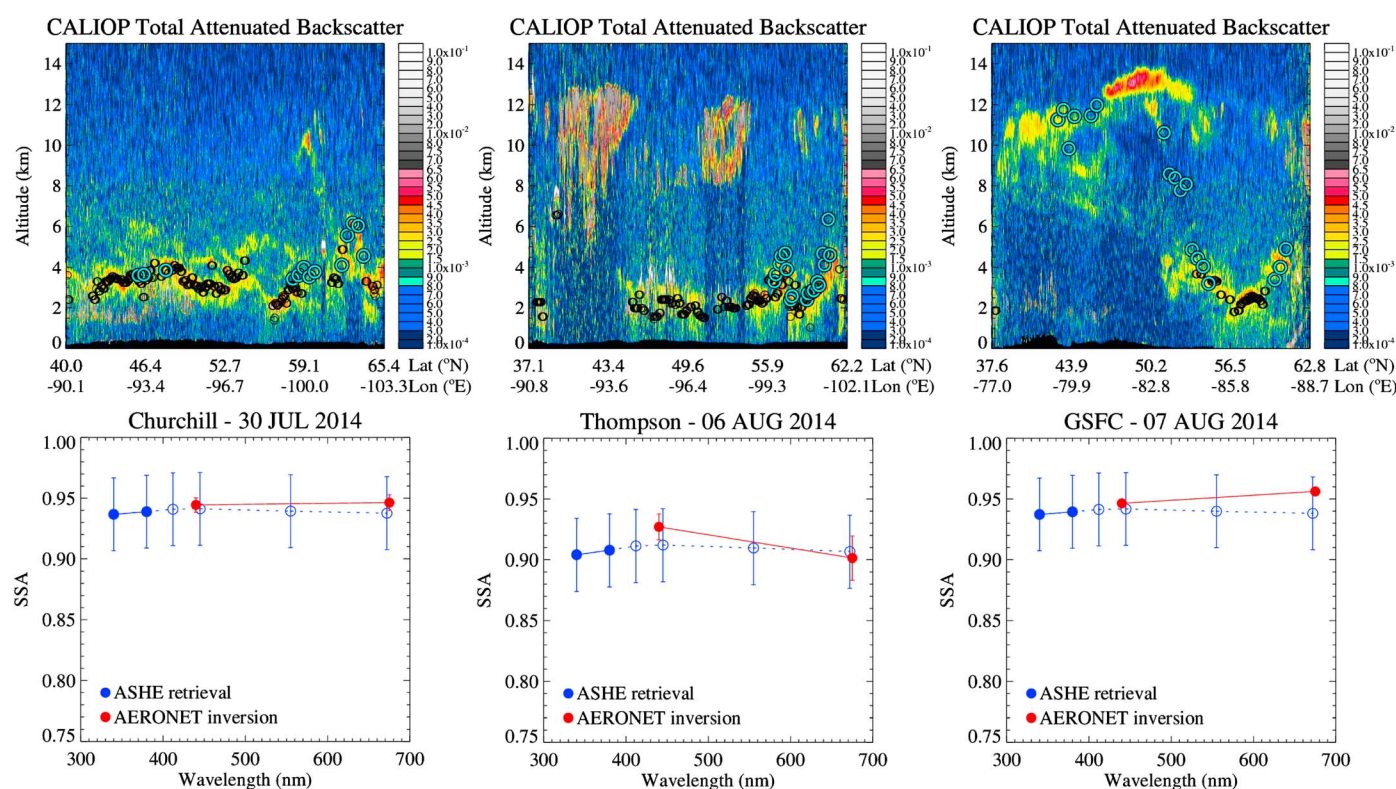


Figure 6. (upper) Comparison of the ATHs between ASHE (cyan circle) and CALIOP observations (black circle) for the smoke plumes over North America, and (lower) the corresponding SSA retrievals compared with the AERONET inversion data for three different cases. The error bars in the SSA from ASHE algorithm show AERONET SSA uncertainty of 0.03, and those from AERONET represent temporal standard deviation within 2 h of VIIRS observation. Open circles in the ASHE-retrieved SSAs are extrapolated values based on the aerosol models used in the forward model.

Figure 6 compares retrieved ATHs with CALIOP observations, and the corresponding SSAs against AERONET inversion data for three different smoke cases observed in various regions over North America to show the robustness of the algorithm. The retrieved variables generally show a high level of correspondence with their counterparts while demonstrating some interesting features. While the smoke aerosols for these cases are generally observed to be below 6 km with strong spatial variability, in some cases they can be seen higher than 10 km (as shown by the CALIOP TAB profiles). The retrieved ATH follows the enhanced TAB signals well even over areas where ATH is not determined by CALIOP observations, mainly due to smoke layers being misidentified as clouds. As shown in the smoke event on 7 August 2014, when there are multiple aerosol layers, the algorithm tends to report intermediate heights between those layers depending on the optical depth of each layer; i.e., shifting toward the layer with higher optical depth is expected. In this case the retrieved height should be considered as the radiatively effective height rather than the top height. Note that for this specific smoke case, the enhanced TAB signals at altitudes higher than 10 km and at latitudes of around 49°N were identified as clouds/stratospheric feature by the CALIOP feature classification product where the VIIRS RGB image showed thick smoke layer (not shown). As shown in Table 4, the retrieved ATHs for the case studies show RMSEs ranging from 0.69 to 1.31 km, which are generally within 30% of the retrieved heights, and MB from 0.25 to 1.13 km for single-layered aerosol events.

Meanwhile, the retrieved 445 nm SSA for the three different cases ranges from 0.91 to 0.94 and is within 0.03 of those from AERONET inversion data, where 0.03 is the uncertainty of the AERONET SSA data. The high agreement between the two products can be achieved when the following conditions are met along the CALIOP swath: accurate AOD retrievals, a representative aerosol model, appropriate aerosol profile, and a sufficient number of collocated pixels. The results for different cases indicate that the spectral SSA of smoke can change significantly, which makes the comparison at longer wavelengths difficult. It is known that the optical properties of smoke, including spectral SSA, show strong regional variations due to the difference

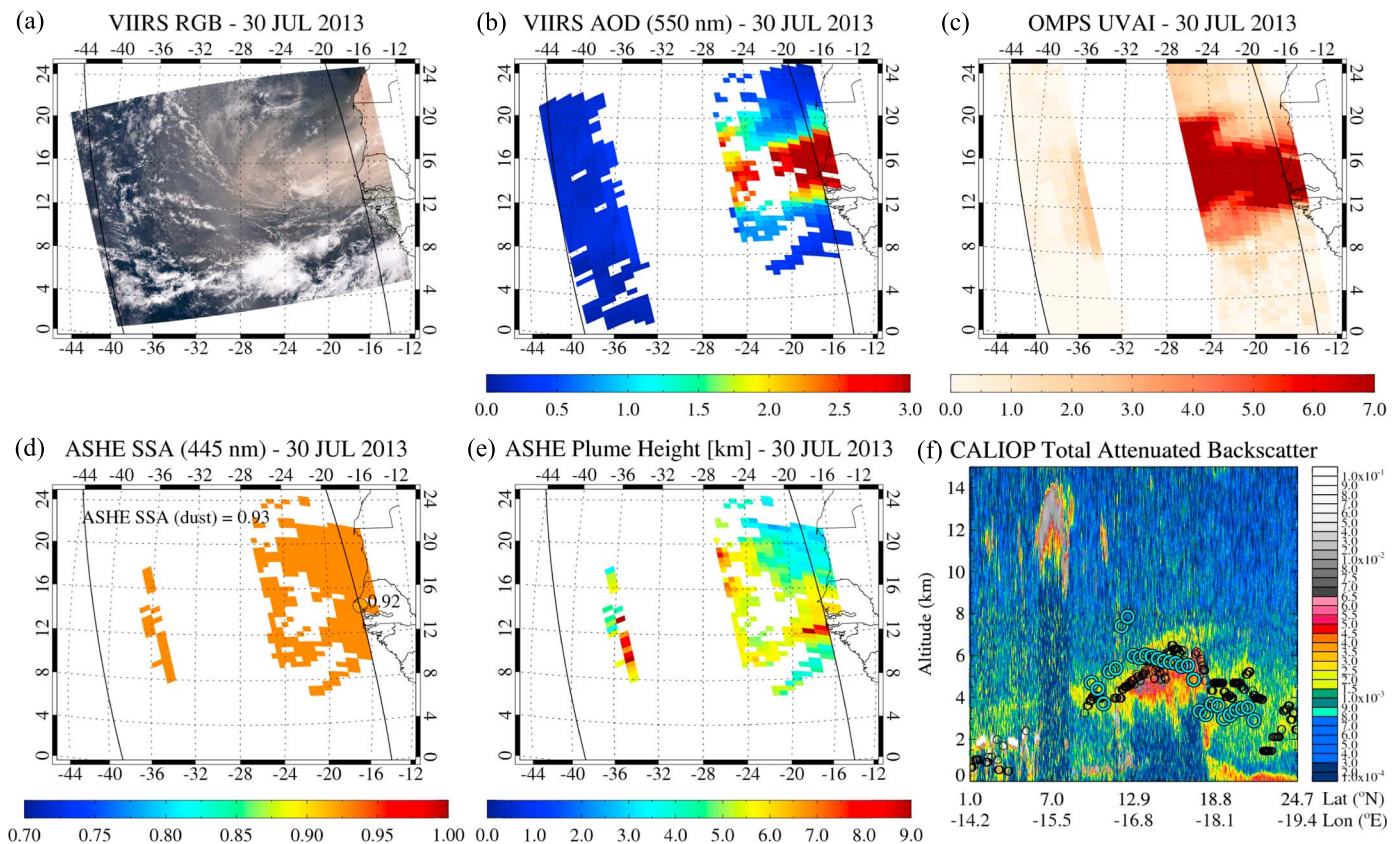


Figure 7. As Figure 5 except for a Saharan dust event observed on 30 July 2013.

in burning characteristics, such as material burned and combustion type [e.g., Dubovik et al., 2002; Reid et al., 2005; Lee et al., 2010a; Sayer et al., 2014a].

4.2. Application to Saharan Dust Over the Atlantic Ocean

This section provides similar analyses to the previous section using Saharan dust cases from June to August 2013. Figure 7 shows an example of a strong dust event observed on 30 July 2013 off the west coast of North Africa. The retrieved AOD of the dust layer is well above 3.0 over a wide area, which is a favorable condition for the ASHE algorithm, and the corresponding UVAI also indicates a strong UV absorption signal. This is a suitable test case to examine the effects of increased pixel size on the retrieval results, as the CALIOP swath passes through the edge of the VIIRS/OMPS swath where the pixel size is large. Although reduced performance is expected, the algorithm resulted in comparable SSA at 445 nm (0.93) to that from the AERONET inversion data at the Dakar site (0.92). This is likely helped by the improved collocation scheme that accurately matches the pixel size between the VIIRS and OMPS products. However, the effects of pixel growth are expected to be larger for pixels containing sharp boundaries of aerosol layers and/or large portions of clouds.

The retrieved ATH generally ranges from 3 to 6 km, while increased ATHs are detected near the sun glint region and around 12°N along the CALIOP swath. The former is likely due to the enhanced UVAI near sun glint (resulting from the Lambertian assumption in the UVAI calculation), while the latter is found to be due to the combined effects of the sharp boundary of the aerosol layer and cloud contamination. The AOD map shows an abrupt change in AOD at those pixels, and the RGB image and TAB profile suggest the presence of low-level clouds below the dust layer. The low-level clouds can enhance the UVAI via multiple scattering between the dust and cloud layers, thereby resulting in a high bias in the retrieved ATH. The VIIRS AOD does not seem to be affected by the cloud contamination due to its higher spatial resolution. Comparisons of ATH between ASHE and CALIOP (Figure 7f) suggest that the ASHE algorithm generally results in a high bias over the cloud contaminated areas, a negligible bias over the thick dust layer, and a low bias where multiple

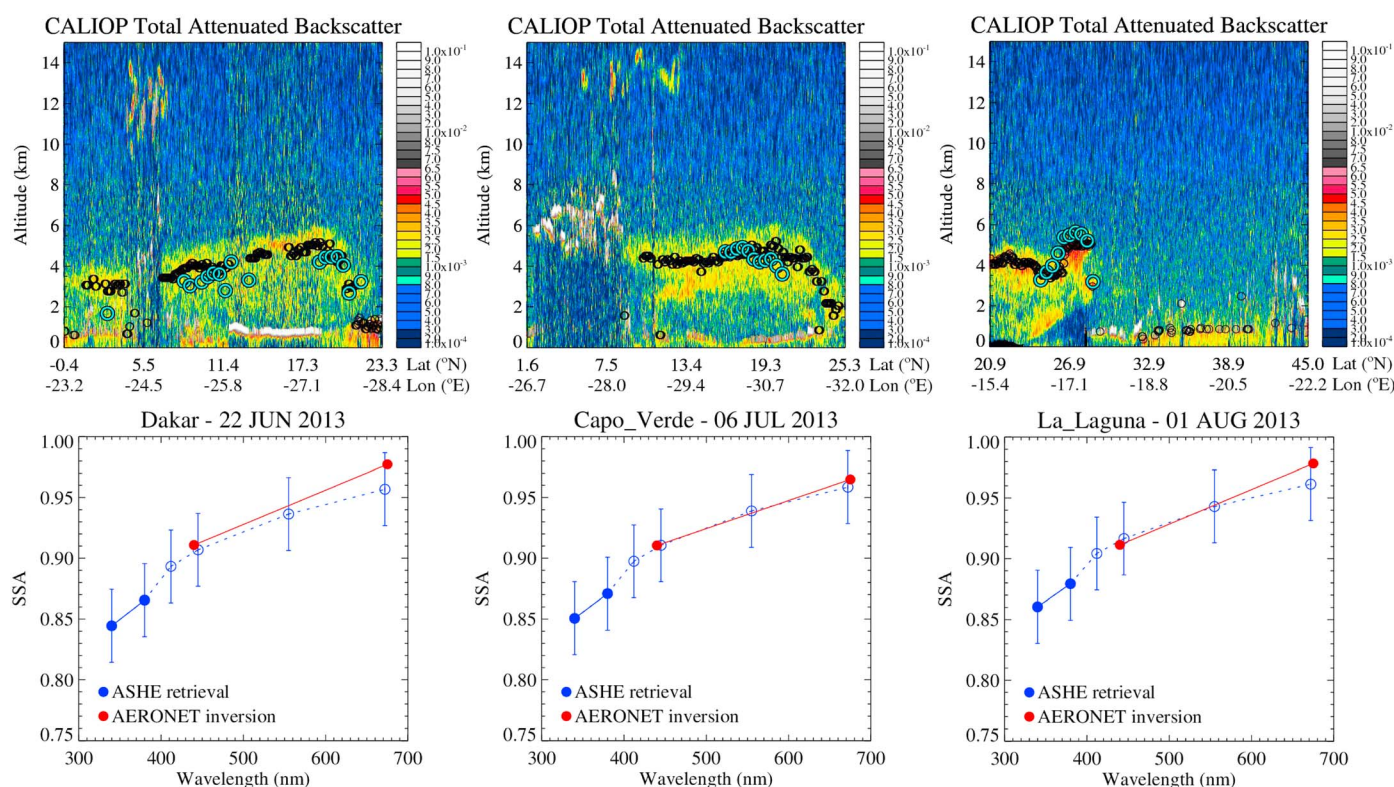


Figure 8. As Figure 6 except for the Saharan dust cases.

aerosol layers are detected. Because the algorithm utilizes a single SSA value and aerosol profile shape within a granule, variability in such parameters could increase errors in the retrieved ATH.

Figure 8 and Table 5 again reveal a high level of correspondence between the ASHE-retrieved parameters (ATH and SSA) and their counterparts. The comparison statistics of ATH between ASHE and CALIOP for dust cases (RMSE ranging from 0.58 to 1.05 km and MB from -0.70 to 0.50 km) are comparable to those of the smoke cases, and the retrieved SSA compares well to the AERONET values. This is remarkable because the dust layers show more complex vertical structure than the smoke cases, which can increase the level of uncertainty. It is inferred that the high level of accuracy is achieved by the higher AOD accuracy over ocean, stronger UVAI sensitivity to dust, and larger plume size. These are optimal to maximize the performance of the ASHE algorithm. The SSA at 440 nm (and potentially at UV wavelengths) of Saharan dust shows smaller temporal variability than the smoke aerosols over North America, which makes the use of an assumed SSA without CALIOP observations for the height retrievals more promising. However, thorough seasonal and regional investigations need to be made before selecting representative SSA values as optical properties of dust can significantly change depending on its source region.

4.3. Uncertainty Estimates

Uncertainty in the retrieved ATH is estimated by calculating retrieval sensitivities to perturbations in the possible error sources: AOD, SSA, aerosol model [FMF and absorption AE (AAE)], aerosol profile shape, cloud

Table 5. As Table 4 Except for Dust Cases

Aerosol Type	Date	Mean ATH (km)		RMSE (km)	MB (km)
		CALIOP	ASHE		
Dust	22 June 2013	3.85	3.52	0.77	-0.38
	06 July 2013	4.72	4.44	0.58	-0.29
	30 July 2013	4.98	4.81	1.05	-0.70
	01 August 2013	4.24	4.59	0.68	0.50

Table 6. Retrieval Errors in ATH According to the Possible Error Sources^a

Error Source	Perturbation	Smoke		Dust	
		ATH = 1 km	ATH = 5 km	ATH = 1 km	ATH = 5 km
AOD (land)	+(0.03 + 20%)	−0.20 (−0.17)	−0.63 (−0.37)	−0.23 (−0.18)	−0.82 (−0.52)
	−(0.03 + 20%)	0.35 (0.37)	1.27 (0.92)	0.45 (0.39)	1.73 (1.23)
AOD (ocean)	+(0.03 + 5%)	−0.09 (−0.06)	−0.29 (−0.14)	−0.11 (−0.07)	−0.38 (−0.20)
	−(0.03 + 5%)	0.13 (0.12)	0.45 (0.28)	0.16 (0.12)	0.61 (0.36)
SSA (land)	+(retrieval error + 0.02)	0.90 (0.79)	3.20 (2.06)	0.73 (0.61)	2.83 (1.73)
	−(retrieval error + 0.02)	−0.38 (−0.35)	−1.63 (−1.40)	−0.43 (−0.37)	−1.55 (−1.27)
SSA (ocean)	+(retrieval error + 0.02)	0.63 (0.56)	2.11 (1.54)	0.44 (0.33)	1.60 (1.13)
	−(retrieval error + 0.02)	−0.30 (−0.25)	−1.23 (−1.06)	−0.28 (−0.23)	−1.03 (−0.81)
FMF	0.3 or 0.2 ^b	0.19 (0.24)	0.65 (0.46)	0.04 (0.07)	−0.50 (−0.34)
AAE	+0.4	−0.38 (−0.46)	−0.49 (−0.51)	−0.25 (−0.28)	−0.40 (−0.39)
	−0.4	0.50 (0.58)	0.58 (0.55)	0.30 (0.32)	0.45 (0.40)
Profile shape	+1 km	^b	0.51 (0.45)	^b	0.52 (0.46)
	−1 km	^b	−0.32 (−0.29)	^b	−0.31 (−0.29)
CF-below	20%	^b	0.18 (0.10)	^b	0.13 (0.05)
CF-above	20%	0.15 (0.04)	−0.26 (−0.37)	0.04 (−0.02)	−0.38 (−0.48)
Aerosol type		−0.67 (−0.47)	1.75 (1.30)	0.11 (0.13)	−1.22 (−0.83)

^aThe median errors derived for the whole geometry node points in the LUTs (total 1539 points) are summarized for ATH of 1 km and 5 km and for AOD of 0.5 and 1.0 (in the parentheses). The errors are represented in km.

^bSee text for details.

fraction (CF), and aerosol type. For this investigation, a “reference” state is assumed to have AOD of 0.5 or 1.0 for moderate to thick aerosol loadings, typical 340 nm SSA of 0.9 for smoke and 0.85 for dust, and ATH of 5 km with geometric thickness of 1 km unless otherwise stated. As the calculated errors were found to depend on observation geometries, the median errors derived for all geometry node points in the LUTs are discussed here. The assumed perturbations are based on the published literature where possible, and reasonable assumptions are made for error sources that are less well documented. Table 6 summarizes the estimated errors in the retrieved ATH for each source of error as described below.

4.3.1. AOD

First of all, the errors due to the uncertainties in AOD are analyzed. Given perturbations of $\pm(0.03 + 0.2\tau)$ over land [Sayer *et al.*, 2013] and $\pm(0.03 + 0.05\tau)$ over ocean [Lee *et al.*, 2012], the median retrieval errors range from −0.82 to 1.73 km (−0.52 to 1.23 km) over land and −0.38 to 0.61 km (−0.20 to 0.36 km) over ocean for AOD of 0.5 (1.0). The positive (negative) bias in AOD corresponds to the negative (positive) bias in ATH. The retrieval errors are generally more sensitive to the errors that result in positive biases since the sensitivity of UVAI to ATH decreases with altitude (due to the height-dependent Rayleigh scattering signals), and the sensitivity to AOD also decreases with AOD (i.e., larger change in UVAI for negative AOD error than positive error) [see de Graaf *et al.*, 2005, Figure 4]. Although UVAI is known to be more sensitive to dust than smoke, smoke shows smaller retrieval errors than dust because AOD of smoke is much higher than that of dust at UV wavelengths due to the smaller particle size (high AE). Note that the retrieval error decreases with AOD.

4.3.2. SSA

It is found that the uncertainty in SSA is a significant source of error. Not only retrieval uncertainty in SSA due to the errors in AOD, but also spatial variability within a VIIRS granule, can contribute to the SSA uncertainty. To account for both of these effects, the retrieval uncertainties in SSA over land and ocean are derived assuming the aforementioned uncertainties in AOD, and an additional uncertainty of 0.02 is assumed to account for the spatial variability. For AOD of 0.5 (1.0), the median errors in ATH range from −1.63 to 3.20 km (−1.40 to 2.06 km) over land and −1.23 to 2.11 km (−1.06 to 1.54 km) over ocean. In contrast to the errors due to AOD, positive (negative) biases in SSA result in positive (negative) errors in the retrieved ATH. In addition, dust shows smaller errors than smoke because of the stronger sensitivity of UVAI to dust than smoke and lower SSA. Although the retrieval uncertainty in SSA plays a significant role, choosing the median SSA among those retrieved along the CALIOP swath effectively alleviates the uncertainty in SSA because the AOD retrieval errors have been found to follow a Gaussian distribution [Sayer *et al.*, 2013]. Thus, increasing the number

of samples in retrieving SSA can significantly reduce the retrieval uncertainty of ATH, in particular over land where the uncertainty of AOD (thus the retrieval uncertainty of SSA) is high.

4.3.3. Aerosol Model

To estimate errors due to the fixed aerosol models, retrieval results are analyzed for perturbations made to both FMF and AAE. For FMF, since the assumed smoke and dust models have rather extreme FMF values (0.85 for smoke and 0.15 for dust), biases are made in one direction, i.e., negative biases of 0.3 for smoke and positive bias of 0.2 for dust. Then, we assume the same amount of error for the opposite direction. The magnitudes of the biases correspond to AE biases of around 0.45, which covers a wide range of AE. The results show that the uncertainty in aerosol size information leads to median errors of 0.34–0.65 km depending on aerosol type and loading. Since biases in FMF are directly related to the biases in AOD at UV wavelengths, a similar tendency to AOD errors is observed (i.e., retrieval bias in the same direction). For AAE, we assume an uncertainty of 0.4, which is an intermediate value between the standard deviation of AAE of smoke aerosols from different source regions [Sayer *et al.*, 2014a] and that of dust [Russell *et al.*, 2010]. The positive (negative) bias in AAE leads to higher (lower) UVAI for a given aerosol loading condition, thereby resulting in negative (positive) bias in ATH. As a result, the uncertainties in AAE are found to contribute additional errors ranging from -0.51 to 0.58 km to the retrieved ATH.

4.3.4. Aerosol Vertical Profile Shape

Using a fixed aerosol profile shape can be a source of error if there is variability in the profile shape spatially within the VIIRS granule. To this end, retrievals are performed assuming an aerosol layer with geometric thickness of 1 or 3 km given UVAI for a reference state with geometric thickness of 2 km. When the thickness is overestimated, the retrieved ATH is biased high by 0.52 km, while it is biased low by 0.32 km when underestimated, without showing strong dependence on the aerosol loading.

4.3.5. Cloud Contamination

To simulate the effects of liquid cloud contamination, synthetic UVAI values were created by linear mixing of the UVAI values calculated assuming cloud-free and cloudy conditions. A gamma size distribution with a mode radius of 4.21 micrometer [d1 model in Tampieri and Tomasi, 1976] and cloud optical depth of 5 are assumed and located at ± 1 km of the aerosol layer for the radiative transfer calculations of cloudy conditions. It is found that clouds above the aerosol layer result in a negative bias in the retrieved ATH by reducing UVAI values, whereas below-aerosol clouds lead to a positive bias due to the increased radiation absorption of the aerosol layer resulting from the enhanced multiple scattering between the cloud and aerosol layers. When assuming 20% cloud contamination, the below-aerosol clouds result in positive biases ranging from 0.05 to 0.18 km, and above-aerosol clouds show negative biases ranging from -0.26 to -0.48 km.

4.3.6. Aerosol Types

The retrieval errors resulting from inaccurate aerosol type (i.e., smoke vs. dust) characterization can be derived by performing the retrieval process using the LUT for the other aerosol type. It is suggested that identifying the aerosol type incorrectly can be a significant source of error, showing the median errors ranging from -1.22 to 1.75 km (-0.83 to 1.30 km) for AOD of 0.5 (1.0). Although the accuracy of the aerosol type detection cannot be quantified at the moment, the errors are expected to be larger over land than over ocean due to the lower accuracy in AE over land.

4.3.7. Height Dependence

The uncertainty in the retrieved ATH is height dependent. The error analysis for various ATHs suggests that the absolute uncertainty tends to increase with ATH, whereas the opposite is true for the fractional uncertainty. Comparison of errors between ATH of 1 km and 5 km shows that the errors for ATH of 5 km are generally three to four times higher (not five times) than those for ATH of 1 km, except for errors due to AAE, cloud contamination, and aerosol type, implying complexity of representing the errors regardless of the height. Note that errors due to profile shape and CF-below could not be derived for ATH of 1 km as the reference profile spans from the surface to 1 km, such that different geometric thickness does not change the profile shape, and cloud cannot be defined below the aerosol layer.

4.3.8. Surface Elevation

The uncertainty of using the two nodes (0 km and 3 km) and linear interpolation when accounting for the effect of surface elevation is examined. For the typical smoke and dust cases at 5 km, the linear interpolation results in uncertainty of ~ 50 m for surface elevation of 0.5 km and ~ 300 m for 1.5 km without showing strong dependence on aerosol type and AOD. Because the uncertainty can be reduced further if increasing the number of nodes, it is not included in the root-sum-square error described below.

Table 7. The Median Errors in ATH Calculated as Root-Sum-Square of the Errors Presented in Table 6 for Various Scenarios^{a,b}

Possible Scenarios		Smoke		Dust	
		Land	Ocean	Land	Ocean
S1	CF-below	−0.85 ~ 4.00 (−0.98 ~ 2.74)	0.86 ~ 2.96 (0.03 ~ 2.21)	−2.25 ~ 3.20 (−1.71 ~ 2.08)	−1.78 ~ 1.48 (−1.32 ~ 1.10)
	CF-above	−0.91 ~ 3.98 (−1.05 ~ 2.71)	0.80 ~ 2.94 (−0.38 ~ 2.17)	−2.28 ~ 3.18 (−1.78 ~ 2.02)	−1.83 ~ 1.42 (−1.40 ~ 0.99)
S2	CF-below	1.02 ~ 2.83 (0.50 ~ 2.23)	1.17 ~ 2.57 (0.61 ~ 2.05)	−1.75 ~ 1.79 (−1.27 ~ 1.42)	−1.59 ~ 0.76 (−1.18 ~ 0.80)
	CF-above	0.97 ~ 2.82 (0.32 ~ 2.19)	1.12 ~ 2.55 (0.47 ~ 2.01)	−1.79 ~ 1.74 (−1.36 ~ 1.34)	−1.64 ~ 0.65 (−1.27 ~ 0.63)
S3	CF-below	−1.95 ~ 3.59 (−1.63 ~ 2.41)	−1.53 ~ 2.39 (−1.30 ~ 1.78)	−1.89 ~ 3.43 (−1.49 ~ 2.24)	−1.30 ~ 1.92 (−1.02 ~ 1.38)
	CF-above	−1.97 ~ 3.58 (−1.67 ~ 2.38)	−1.56 ~ 2.37 (−1.35 ~ 1.74)	−1.93 ~ 3.40 (−1.57 ~ 2.18)	−1.36 ~ 1.87 (−1.13 ~ 1.29)
S4	CF-below	−1.42 ~ 2.23 (−1.20 ~ 1.81)	−1.30 ~ 1.89 (−1.15 ~ 1.58)	−1.25 ~ 2.17 (−0.97 ~ 1.65)	−1.02 ~ 1.44 (−0.84 ~ 1.15)
	CF-above	−1.45 ~ 2.21 (−1.26 ~ 1.77)	−1.34 ~ 1.86 (−1.21 ~ 1.53)	−1.31 ~ 2.13 (−1.08 ~ 1.57)	−1.09 ~ 1.38 (−0.97 ~ 1.04)
S5	Clear-sky	−1.43 ~ 2.22 (−1.20 ~ 1.80)	−1.32 ~ 1.88 (−1.15 ~ 1.58)	−1.26 ~ 2.16 (−0.97 ~ 1.64)	−1.02 ~ 1.43 (−0.84 ~ 1.15)

^aThe errors are for typical smoke and dust layers at 5 km with geometric thickness of 1 km for AOD of 0.5 and 1.0 km (in the parentheses) and represented in km.

^bS1: including all of the error sources in Table 6, S2: w/o SSA retrieval error, S3: w/o aerosol type detection error, S4: w/o SSA retrieval error and aerosol type detection error, S5: w/o SSA retrieval error, aerosol type detection error, and cloud contamination.

The root-sum-square errors due to the aforementioned sources of error are summarized in Table 7 for typical smoke and dust layers with ATH of 5 km. Because the uncertainty in aerosol type could not be quantified at the moment and the retrieval errors in SSA could change for different conditions, the errors with and without the parameters are provided. As a result, the uncertainty in the retrieved aerosol height is estimated from −1.20 to 1.80 km over land and from −1.15 to 1.58 km over ocean when favorable conditions are met, i.e., high aerosol loading (AOD of ~1.0), accurate aerosol type detection, a sufficient number of data points for the SSA retrievals, and cloud-free condition (scenario S5). For ATH of 1 km, the uncertainties decrease to −0.57 to 0.86 km and −0.55 to 0.78 km over land and ocean, respectively. Intermediate values are expected for ATHs between the two. Although there are a lot of complexities in the retrieval uncertainties for various scenarios, the uncertainties are generally smaller for dust, higher AOD, and ocean surfaces than the respective counterparts. It is found that in the worst case scenario (S1), the maximum uncertainty can be as high as 80% for moderate smoke layers over land, which motivates us to develop, in ongoing work, a sophisticated quality assurance procedure to inform users to use appropriate subsets of the data for different applications.

5. Summary and Discussions

We have presented an improved ASHE algorithm to provide aerosol height information over wide areas with the representative SSA by synergistic use of aerosol products from multiple satellite sensors. The VIIRS and OMPS sensors were used in place of MODIS and OMI, respectively, illustrating the potential to extend the data record from this algorithm beyond the EOS era. One of the major updates made to the algorithm was to include nonspherical dust properties in the forward models for both AOD retrievals and UVAI calculations in order to extend the application of the algorithm to dust layers as well as smoke. In addition, refinements were made to the collocation scheme, aerosol profile shapes, and treatment of surface elevation, which help to further improve the retrieval performance.

We presented results for several smoke and dust cases observed in summer in North America and the Atlantic Ocean, respectively, to evaluate the performance of the algorithm. When favorable conditions were met (i.e., single aerosol layer, heavy aerosol loading, small spatial variability in SSA, sufficient number of collocation for SSA retrieval, and cloud-free condition), the algorithm performed well for both smoke and dust cases without showing obvious systematic biases. This implies that the assumptions made in the algorithm, such as spatial homogeneity in SSA and optical properties for smoke and dust, hold well for the test cases. However, it would be challenging to apply the algorithm to aerosol events originating from multiple source regions that can show variable optical properties within a granule, dust or smoke layers mixed with other aerosol types or each other, and/or the aerosols of which optical properties significantly differ from the assumed aerosol models. It is also known that the optical properties of smoke (both SSA and AE) can change rapidly during the aging process [Reid *et al.*, 2005]. In addition, the present algorithm showed a weakness for multilayered aerosol events, for which it tends to report intermediate heights between the layers, due to the limited sensitivity of passive sensors to such cases. Major sources of error were found to be the retrieval accuracy of AOD, FMF, and SSA, spatial variability in SSA and AAE (thus spectral SSA), cloud contamination in the large

OMPS pixel, and accuracy of aerosol type detection. The error analysis revealed that the estimated error in the retrieved ATH for typical single-layered aerosol events ranges from 1.20 to 1.80 km over land and 1.15 to 1.58 km over ocean when favorable conditions are met. Multilayered aerosols, inaccurate aerosol type detection, and biased SSA retrievals were found to further increase the uncertainties. Therefore, a careful quality assurance procedure will be developed to guide users to appropriate data sets according to their application purposes.

Since the ASHE algorithm utilizes Level 2 aerosol products, it can directly benefit from future improvements to each data set. The operational NASA VIIRS Deep Blue data set plans to include the nonspherical dust properties used in this study for better performance in retrieving optical properties of dust in the over-ocean algorithm, and a preliminary investigation of using the same dust models in the land algorithm is underway as well. Improvements in the AE product are desirable to use more accurate aerosol models in the retrieval process, which will further improve the retrieval accuracy. One of the synergies that can be made between the Deep Blue and ASHE algorithms is that the retrieved SSA from ASHE can be used to inform aerosol model selection in the Deep Blue algorithm. This can possibly improve the low bias in Deep Blue AOD which has been observed for MODIS in some high-AOD regimes [Sayer *et al.*, 2013, 2014b]. The ASHE algorithm can benefit from the improved AOD recursively.

As seen by the case study over ocean, sun glint affects UVAI, resulting in overestimation in the retrieved ATH. Including the effects of ocean surface bidirectional reflectance distribution function in calculating UVAI or correcting for the effect in the OMPS-derived values is desirable to improve the results near the glint region. For CALIOP, it was found that the feature classification tends to identify heavy smoke layers as clouds, causing a sampling issue when retrieving SSA for such cases. The planned version 4 CALIOP data are expected to address this issue, and use of the color ratio between 532 and 1064 nm might help recover some dense smoke layers.

As noted previously, spatial coverage could be expanded by removing the requirement for CALIOP observations, at the cost of increased errors (as SSA and profile shape would be assumed rather than retrieved). This has not been done at the present time due to arbitrariness in the choice of SSA. However, we envisage that after larger-scale ASHE processing, an ASHE-retrieved SSA climatology could be constructed and be used as a constraint on the regional/seasonal variation of dust and smoke SSA. With the aforementioned improvements and operational processing planned in the future, the present algorithm is expected to help provide a more complete picture of global aerosol height together with the existing complementary products from active (e.g., CALIOP) and passive [e.g., (A)ATSR and MISR] spaceborne sensors.

Acknowledgments

This project is funded by the NASA's EOS program, managed by H. Maring. The VIIRS, OMPS, and CALIOP science teams are gratefully acknowledged for their efforts to create and maintain the data records used in this investigation. We thank the PIs and managers (I. Abboud, M. Anderson, J. C. Antuqua Marrero, W. P. Arnott, V. E. Cachorro Revilla, C. Coburn, A. L. Contreras, A. Cooper, J. Csavina, P. Disterhoft, V. Fioletov, G. A. Fouts, R. Frouin, H. Fuelberg, G. Gimmestad, B. Gingrey, E. Gonzalez, W. M. Hao, J. Herman, R. M. Hoff, B. N. Holben, P. Ionov, M. Ivey, F. Javier, S. Jones, T. Kampe, K. Knupp, G. Labow, B. Lefer, C. Lehmann, G. Lesins, D. Moore, A. H. Omar, N. O'Neill, T. H. Painter, S. Piazzolla, B. Pierce, A. Predoi-Cross, K. Repasky, A. Royer, G. P. Robertson, J. A. Shaw, J. Sherman, G. Stensaa, J. Stutz, D. Tanré, M. Tzortziou, J. van den Bosch, R. Wagener, C. Walthall, and J. Zhang) for establishing and maintaining the AERONET sites. Ping Yang at Texas A&M University is also acknowledged for providing the single-scattering property database for tri-axial ellipsoidal particles. The VIIRS data were obtained from the NASA Atmosphere Science Investigator-led Processing Systems (SIPS) (sips.ssec.wisc.edu/flo/search/), the OMPS data from the website of the NASA OMPS science team (<https://ozoneaq.gsfc.nasa.gov/data/omps/>), the CALIOP data from the NASA Langley Research Center Atmospheric Science Data Center (<https://eosweb.larc.nasa.gov/order-data/>), and the AERONET data from the AERONET website (<http://aeronet.gsfc.nasa.gov>).

References

- Ackerman, A. S., O. B. Toon, D. E. Stevens, A. J. Heymsfield, V. Ramanathan, and E. J. Welton (2000), Reduction of tropical cloudiness by soot, *Science*, *288*(5468), 1042–1047, doi:10.1126/science.288.5468.1042.
- Cao, C., J. Xiong, S. Blonski, Q. Liu, S. Uprety, X. Shao, Y. Bai, and F. Weng (2013), Suomi NPP VIIRS sensor data record verification, validation, and long-term performance monitoring, *J. Geophys. Res. Atmos.*, *118*, 11,664–11,678, doi:10.1002/2013JD020418.
- Choi, J.-O., and C. E. Chung (2014), Sensitivity of aerosol direct radiative forcing to aerosol vertical profile, *Tellus B*, *66*, doi:10.3402/tellusb.v66.24376.
- Dave, J. V. (1972), Development of programs for computing characteristics of ultraviolet radiation, *Vector Case, Tech. Rep.*, IBM Corp., Fed. Syst. Div., Gaithersburg, Md.
- de Graaf, M., P. Stammes, O. Torres, and R. B. A. Koelemeijer (2005), Absorbing Aerosol Index: Sensitivity analysis, application to GOME and comparison with TOMS, *J. Geophys. Res.*, *110*, D01201, doi:10.1029/2004JD005178.
- Diner, D. J., et al. (1998), Multi-angle Imaging SpectroRadiometer (MISR)—Instrument description and experiment overview, *IEEE Trans. Geosci. Remote Sens.*, *36*(4), 1072–1087, doi:10.1109/36.700992.
- Dubovik, O., and M. D. King (2000), A flexible inversion algorithm for retrieval of aerosol optical properties from Sun and sky radiance measurements, *J. Geophys. Res.*, *105*(D16), 20,673–20,696, doi:10.1029/2000JD900282.
- Dubovik, O., A. Smirnov, B. N. Holben, M. D. King, Y. J. Kaufman, T. F. Eck, and I. Slutsker (2000), Accuracy assessments of aerosol optical properties retrieved from Aerosol Robotic Network (AERONET) Sun and sky radiance measurements, *J. Geophys. Res.*, *105*(D8), 9791–9806, doi:10.1029/2000JD900040.
- Dubovik, O., B. Holben, T. F. Eck, A. Smirnov, Y. J. Kaufman, M. D. King, D. Tanré, and I. Slutsker (2002), Variability of absorption and optical properties of key aerosol types observed in worldwide locations, *J. Atmos. Sci.*, *59*(3), 590–608.
- Dubovik, O., et al. (2006), Application of spheroid models to account for aerosol particle nonsphericity in remote sensing of desert dust, *J. Geophys. Res.*, *111*, D11208, doi:10.1029/2005JD006619.
- Fisher, D., J.-P. Muller, and V. N. Yershov (2014), Automated stereo retrieval of smoke plume injection heights and retrieval of smoke plume masks from AATSR and their assessment with CALIPSO and MISR, *IEEE Trans. Geosci. Remote Sens.*, *52*(2), 1249–1258, doi:10.1109/TGRS.2013.2249073.
- Giglio, L., J. Descloitres, C. O. Justice, and Y. J. Kaufman (2003), An enhanced contextual fire detection algorithm for MODIS, *Remote Sens. Environ.*, *87*, 273–282, doi:10.1016/S0034-4257(03)00184-6.

- Hansen, J., M. Sato, and R. Ruedy (1997), Radiative forcing and climate response, *J. Geophys. Res.*, *102*(D6), 6831–6864, doi:10.1029/96JD03436.
- Herman, J., P. Bhartia, O. Torres, C. Hsu, C. Seftor, and E. Celarier (1997), Global distribution of UV-absorbing aerosols from Nimbus 7/TOMS data, *J. Geophys. Res.*, *102*(D14), 16,911–16,922, doi:10.1029/96JD03680.
- Holben, B. N., et al. (1998), AERONET—A federated instrument network and data archive for aerosol characterization, *Remote Sens. Environ.*, *66*(1), 1–16, doi:10.1016/S0034-4257(98)00031-5.
- Hsu, N. C., J. R. Herman, P. K. Bhartia, C. J. Seftor, O. Torres, A. M. Thompson, J. F. Gleason, T. F. Eck, and B. N. Holben (1996), Detection of biomass burning smoke from TOMS measurements, *Geophys. Res. Lett.*, *23*(7), 745–748, doi:10.1029/96GL00455.
- Hsu, N. C., J. R. Herman, O. Torres, B. N. Holben, D. Tanre, T. F. Eck, A. Smirnov, B. Chatenet, and F. Lavenu (1999), Comparison of the TOMS aerosol index with Sun-photometer aerosol optical thickness: Results and applications, *J. Geophys. Res.*, *104*(D6), 6269–6279, doi:10.1029/1998JD00086.
- Hsu, N. C., M.-J. Jeong, C. Bettenhausen, A. M. Sayer, R. Hansell, C. S. Seftor, J. Huang, and S.-C. Tsay (2013), Enhanced Deep Blue aerosol retrieval algorithm: The second generation, *J. Geophys. Res. Atmos.*, *118*, 9296–9315, doi:10.1002/jgrd.50712.
- Jeong, M.-J., and N. C. Hsu (2008), Retrievals of aerosol single-scattering albedo and effective aerosol layer height for biomass-burning smoke: Synergy derived from “A-Train” sensors, *Geophys. Res. Lett.*, *35*, L24801, doi:10.1029/2008GL036279.
- Jeong, M.-J., and Z. Li (2005), Quality, compatibility, and synergy analyses of global aerosol products derived from the advanced very high resolution radiometer and Total Ozone Mapping Spectrometer, *J. Geophys. Res.*, *110*, D10S08, doi:10.1029/2004JD004647.
- Kahn, R. A., Y. Chen, D. L. Nelson, F.-Y. Leung, Q. Li, D. J. Diner, and J. A. Logan (2008), Wildfire smoke injection heights: Two perspectives from space, *Geophys. Res. Lett.*, *35*, L04809, doi:10.1029/2007GL032165.
- Kim, J., J. Lee, H. Lee, A. Higuchi, T. Takemura, and C. Song (2007), Consistency of the aerosol type classification from satellite remote sensing during the Atmospheric Brown Cloud-East Asia Regional Experiment campaign, *J. Geophys. Res.*, *112*, D22S33, doi:10.1029/2006JD008201.
- Koren, I., J. V. Martins, L. A. Remer, and H. Afargan (2008), Smoke invigoration versus inhibition of clouds over the Amazon, *Science*, *321*(5891), 946–949, doi:10.1126/science.1159185.
- Lee, J., J. Kim, C. H. Song, S. B. Kim, Y. Chun, B. J. Sohn, and B. N. Holben (2010a), Characteristics of aerosol types from AERONET sunphotometer measurements, *Atmos. Environ.*, *44*(26), 3110–3117, doi:10.1016/j.atmosenv.2010.05.035.
- Lee, J., J. Kim, C. H. Song, J.-H. Ryu, Y.-H. Ahn, and C. K. Song (2010b), Algorithm for retrieval of aerosol optical properties over the ocean from the Geostationary Ocean Color Imager, *Remote Sens. Environ.*, *114*(5), 1077–1088, doi:10.1016/j.rse.2009.12.021.
- Lee, J., J. Kim, P. Yang, and N. C. Hsu (2012), Improvement of aerosol optical depth retrieval from MODIS spectral reflectance over the global ocean using new aerosol models archived from AERONET inversion data and tri-axial ellipsoidal dust database, *Atmos. Chem. Phys.*, *12*(15), 7087–7102, doi:10.5194/acp-12-7087-2012.
- Lee, J., N. C. Hsu, C. Bettenhausen, and A. M. Sayer (2013), Retrieval of aerosol optical depth under thin cirrus from MODIS: Application to an ocean algorithm, *J. Geophys. Res. Atmos.*, *118*, 10,111–10,124, doi:10.1002/jgrd.50806.
- Lee, J., J. Kim, and Y. Lee (2014), Simultaneous retrieval of aerosol properties and clear-sky direct radiative effect over the global ocean from MODIS, *Atmos. Environ.*, *92*, 309–317, doi:10.1016/j.atmosenv.2014.04.021.
- Levy, R. C., S. Mattoo, L. A. Munchak, L. A. Remer, A. M. Sayer, F. Patadia, and N. C. Hsu (2013), The Collection 6 MODIS aerosol products over land and ocean, *Atmos. Meas. Tech.*, *6*(11), 2989–3034, doi:10.5194/amt-6-2989-2013.
- Meloni, D., A. di Sarra, T. Di Iorio, and G. Fiocco (2005), Influence of the vertical profile of Saharan dust on the visible direct radiative forcing, *J. Quant. Spectrosc. Radiat. Transfer*, *93*(4), 397–413, doi:10.1016/j.jqsrt.2004.08.035.
- Meng, Z., P. Yang, G. W. Kattawar, L. Bi, K. N. Liou, and I. Laszlo (2010), Single-scattering properties of tri-axial ellipsoidal mineral dust aerosols: A database for application to radiative transfer calculations, *J. Aerosol Sci.*, *41*, 501–512, doi:10.1016/j.jaerosci.2010.02.008.
- Mishra, A. K., K. Klingmueller, E. Fredj, J. Lelieveld, Y. Rudich, and I. Koren (2014), Radiative signature of absorbing aerosol over the eastern Mediterranean basin, *Atmos. Chem. Phys.*, *14*(14), 7213–7231, doi:10.5194/acp-14-7213-2014.
- Nelson, D. L., M. J. Garay, R. A. Kahn, and B. A. Dunst (2013), Stereoscopic height and wind retrievals for aerosol plumes with the MISR Interactive Explorer (MINX), *Remote Sens.*, *5*(9), 4593–4628, doi:10.3390/rs5094593.
- Omar, A. H., et al. (2009), The CALIPSO automated aerosol classification and lidar ratio selection algorithm, *J. Atmos. Oceanic Technol.*, *26*(10), 1994–2014, doi:10.1175/2009JTECHA1231.1.
- Penner, J. E., S. Y. Zhang, and C. C. Chuang (2003), Soot and smoke aerosol may not warm climate, *J. Geophys. Res.*, *108*(D21), 4657, doi:10.1029/2003JD003409.
- Reid, J. S., T. F. Eck, S. A. Christopher, R. Koppmann, O. Dubovik, D. P. Eleuterio, B. N. Holben, E. A. Reid, and J. Zhang (2005), A review of biomass burning emissions part III: Intensive optical properties of biomass burning particles, *Atmos. Chem. Phys.*, *5*, 827–849.
- Russell, P. B., R. W. Bergstrom, Y. Shinozuka, A. D. Clarke, P. F. DeCarlo, J. L. Jimenez, J. M. Livingston, J. Redemann, O. Dubovik, and A. Strawa (2010), Absorption Angstrom exponent in AERONET and related data as an indicator of aerosol composition, *Atmos. Chem. Phys.*, *10*(3), 1155–1169.
- Samset, B. H., and G. Myhre (2011), Vertical dependence of black carbon, sulphate and biomass burning aerosol radiative forcing, *Geophys. Res. Lett.*, *38*, L24802, doi:10.1029/2011GL049697.
- Sayer, A. M., N. C. Hsu, C. Bettenhausen, Z. Ahmad, B. N. Holben, A. Smirnov, G. E. Thomas, and J. Zhang (2012), SeaWiFS Ocean Aerosol Retrieval (SOAR): Algorithm, validation, and comparison with other data sets, *J. Geophys. Res.*, *117*, D03206, doi:10.1029/2011JD016599.
- Sayer, A. M., N. C. Hsu, C. Bettenhausen, and M.-J. Jeong (2013), Validation and uncertainty estimates for MODIS Collection 6 “Deep Blue” aerosol data, *J. Geophys. Res. Atmos.*, *118*, 7864–7872, doi:10.1002/jgrd.50600.
- Sayer, A. M., N. C. Hsu, T. F. Eck, A. Smirnov, and B. N. Holben (2014a), AERONET-based models of smoke-dominated aerosol near source regions and transported over oceans, and implications for satellite retrievals of aerosol optical depth, *Atmos. Chem. Phys.*, *14*(20), 11,493–11,523, doi:10.5194/acp-14-11493-2014.
- Sayer, A. M., L. A. Munchak, N. C. Hsu, R. C. Levy, C. Bettenhausen, and M.-J. Jeong (2014b), MODIS Collection 6 aerosol products: Comparison between Aqua’s e-Deep Blue, Dark Target, and “merged” data sets, and usage recommendations, *J. Geophys. Res. Atmos.*, *119*, 13,965–13,989, doi:10.1002/2014JD022453.
- Seftor, C. J., G. Jaross, M. Kowitz, M. Haken, J. Li, and L. E. Flynn (2014), Postlaunch performance of the Suomi National Polar-orbiting Partnership Ozone Mapping and Profiler Suite (OMPS) nadir sensors, *J. Geophys. Res. Atmos.*, *119*, 4413–4428, doi:10.1002/2013JD020472.
- Smirnov, A., B. N. Holben, T. F. Eck, O. Dubovik, and I. Slutsker (2000), Cloud-screening and quality control algorithms for the AERONET database, *Remote Sens. Environ.*, *73*(3), 337–349.
- Song, W., K.-U. Hess, D. E. Damby, F. B. Wadsworth, Y. L. Lavallee, C. C. Cimorelli, and D. B. Dingwell (2014), Fusion characteristics of volcanic ash relevant to aviation hazards, *Geophys. Res. Lett.*, *41*, 2326–2333, doi:10.1002/2013GL059182.
- Spurr, R. (2006), VLIDORT: A linearized pseudo-spherical vector discrete ordinate radiative transfer code for forward model and retrieval studies in multilayer multiple scattering media, *J. Quant. Spectrosc. Radiat. Transfer*, *102*(2), 316–342, doi:10.1016/j.jqsrt.2006.05.005.

- Tampieri, F., and C. Tomasi (1976), Size distribution models of fog and cloud droplets in terms of modified gamma function, *Tellus*, 28(4), 333–347.
- Torres, O., P. K. Bhartia, J. R. Herman, Z. Ahmad, and J. Gleason (1998), Derivation of aerosol properties from satellite measurements of backscattered ultraviolet radiation: Theoretical basis, *J. Geophys. Res.*, 103(D18), 23,321–23,321, doi:10.1029/98JD02709.
- Torres, O., C. Ahn, and Z. Chen (2013), Improvements to the OMI near-UV aerosol algorithm using A-train CALIOP and AIRS observations, *Atmos. Meas. Tech.*, 6(11), 3257–3270, doi:10.5194/amt-6-3257-2013.
- van Donkelaar, A., R. V. Martin, M. Brauer, R. Kahn, R. Levy, C. Verduzco, and P. J. Villeneuve (2010), Global estimates of ambient fine particulate matter concentrations from satellite-based aerosol optical depth: Development and application, *Environ. Health Perspect.*, 118(6), 847–855, doi:10.1289/ehp.0901623.
- Williams, J., M. de Reus, R. Krejci, H. Fischer, and J. Strom (2002), Application of the variability-size relationship to atmospheric aerosol studies: Estimating aerosol lifetimes and ages, *Atmos. Chem. Phys.*, 2, 133–145.
- Winker, D. M., W. H. Hunt, and M. J. McGill (2007), Initial performance assessment of CALIOP, *Geophys. Res. Lett.*, 34, L19803, doi:10.1029/2007GL030135.
- Zhang, L., Q. B. Li, Y. Gu, K. N. Liou, and B. Meland (2013), Dust vertical profile impact on global radiative forcing estimation using a coupled chemical-transport-radiative-transfer model, *Atmos. Chem. Phys.*, 13(14), 7097–7114, doi:10.5194/acp-13-7097-2013.